Highly Efficient Ultraviolet Harmonic Generation at a Nonlinear Crystal Interface

Yan Guan,[1,‡] Yujia Wu,[1,‡] Yuanlin Zheng,[1,2] Haigang Liu,[1,*] and Xianfeng Chen[1,2,3,†]

[1] *State Key Laboratory of Advanced Optical Communication Systems and Networks, School of Physics and Astronomy, Shanghai Jiao Tong University, Shanghai 200240, China*

[2] *Shanghai Research Center for Quantum Sciences, Shanghai 201315, China*

[3] *Collaborative Innovation Center of Light Manipulations and Applications, Shandong Normal University, Jinan 250358, China*

(Received 23 January 2022; revised 8 December 2022; accepted 1 May 2023; published 2 June 2023)

High conversion efficiency is vital for the acquisition of UV light through nonlinear processes. Here, we investigate an alternative method to realize highly efficient second-harmonic generation (SHG) based on the interface of β barium metaborate (βBBO) and magnesium-doped lithium niobate (MgO:LN). Theoretical simulations indicate that the SHG efficiency of our method is significantly higher than other phase-matching conditions. In the experiment, we demonstrate that higher conversion efficiency can be realized compared with only employing a single BBO crystal. Besides, the shortest output wavelength of SHG can reach 205 nm in our method. The method proposed here can open another way for the integrated ultraviolet laser and may promote the development of UV micromachining in the future.

DOI: 10.1103/PhysRevApplied.19.064009

I. INTRODUCTION

UV coherent light can be widely applied in biomedicine [1–5], nanofabrication [6–10], semiconductor processes [11–14], ceramic manufacturing [15–17], imagery [18–22], etc. The most common method to directly generate UV light is excimer laser [23]. Since it was invented in 1970, a series of noble gases have been employed to generate UV light for different wavelength and power demands [24]. Although UV lasers based on noble gases can provide high average power and various wavelengths, they always have high energy consumption and cumbersome facility [25]. In recent years, all-solid-state lasers have become one of the most popular candidates for providing UV light [26,27]. They are superior in small volume, low consumption, and high reliability. The key step to realize an all-solid-state UV laser is the nonlinear frequency-conversion process based on nonlinear materials [28]. Usually, the conversion efficiency sharply decreases when the expected harmonic wavelength approaches the deep ultraviolet (DUV) or vacuum ultraviolet (VUV) waveband. It is mainly limited by strong material absorption within the UV waveband and phase mismatching caused by high refractive index [29,30]. Consequently, exploring alternative phase-matching methods or potential nonlinear materials to promote nonlinear conversion efficiency is highly desired for the development of UV lasers.

In previous researches, nonlinear boundaries, including domain-wall structure and boundary of nonlinear crystal are potential alternatives to increase nonlinear conversion efficiency because of their local effect on the nonlinear polarization wave. Cherenkov second-harmonic generation (CSHG) enhancement by using local effect was discussed at domain walls of ferroelectric crystal [31,32]. Then, it was investigated at the surface of single-domain crystal, which was considered as the modulation of the nonlinear Smith-Purcell effect [33]. Subsequently, a more general interface model was proposed to investigate the nonlinear enhancement effect [34]. They theoretically demonstrate that a higher enhancement effect can be obtained by choosing the sharper modulation of $\chi^{(2)}$. Besides, a unified approach was proposed to investigate the modulated nonlinear processes, such as CSHG, nonlinear Raman-Nath, and nonlinear Bragg diffraction stimulated from nonlinear domain walls and interfaces [35]. This theory was also extended to deal with nonlinear processes in nonlinear photonic crystals [36,37]. Further, a special CSHG utilizing total reflection on the inner surface of the crystal to compensate for phase mismatching was also reported as another efficient method [38].

All these works mentioned above realize SHG enhancement in visible wavebands. As for UV harmonic generation, it has been reported that CSHG at 325 nm based

*liuhaigang@sjtu.edu.cn
†xfchen@sjtu.edu.cn
‡These authors contributed equally to this work.

on the nonlinear boundary was substantially enhanced [39,40]. However, such nonlinear Cherenkov radiation is still a phase-mismatching process, so it becomes only distinct under the femtosecond pump. Finding a way to take full advantage of nonlinear boundary enhancement and perfect-phase-matching (PPM) will be fundamental to realize high-efficiency and compact DUV or VUV lasers.

In this paper, we propose and investigate a highly efficient frequency-doubling method based on noncollinear PPM along the crystal boundary. We first systematically calculate the conversion efficiency of SHG under different phase-matching conditions. According to theoretical simulations, we choose β barium metaborate bonding with magnesium-doped lithium niobate (BBO-LN) to generate this kind of noncollinear PPM SHG. Then, we compare the nonlinear conversion efficiency between single BBO surface and BBO-LN interface in the experiment to verify the enhancement effect from the difference of $\chi^{(2)}$. We also experimentally compare our method with traditional birefringence phase matching. The result shows that our method works more efficiently.

II. THEORY

To calculate the conversion efficiency of SHG under different conditions, we solve the coupling wave equation in a general form. For the Gaussian beam, Fourier transformation assists deduction of the expression of SHG amplitude [40]. Under paraxial and small signal approximations, the intensity of the SHG spectrum can be written as

$$\begin{aligned} I_2(k_x,z) &= |A_2(k_x,z)|^2 \\ &= \frac{k_2^2 A_1^4}{n_2^4} z^2 \sin c^2\left\{\frac{\left[k_x^2/(2k_2)-\Delta k\right]z}{2}\right\} \\ &\times \left|\int_{-\infty}^{+\infty} d_{\text{eff}} e^{-2x^2/a^2} e^{ik_x x} dx\right|^2, \end{aligned} \tag{1}$$

in which x and z represent the lateral axis and the propagation axis, respectively. k_x is introduced by Fourier transformation to represent spatial frequency. a is the radius of the Gaussian beam. n_2 is the refractive index of material for SHG. A_1 and A_2 are electric field amplitudes of fundamental frequency (FF) wave and SHG, respectively. k_1 and k_2 are wave vectors of FF wave and SHG, respectively. $\Delta_k = 2k_1 - k_2$ represents phase mismatching of this nonlinear process. d_{eff} is the effective nonlinear coefficient that varies according to materials as well as phase-matching conditions. d_{eff} can be expressed as a piecewise function for a nonlinear boundary. Therefore, for SHG stimulated at a nonlinear boundary,

$$\begin{aligned} &\int_{-\infty}^{+\infty} d_{\text{eff}} e^{-2x^2/a^2} e^{ik_x x} dx \\ &= d\left[(C_1+C_2)\sqrt{\frac{\pi}{8}} a e^{-a^2k_x^2/8}\right. \\ &+ C_2 \frac{a}{\sqrt{2}} e^{-a^2k_x^2/4} D\left(\frac{iak_x}{\sqrt{8}}\right) \\ &\left. - C_1 \frac{a}{\sqrt{2}} e^{2h^2/a^2 + ihk_x - a^2k_x^2/4} \cdot D\left(\frac{\sqrt{2}h}{a} + \frac{iak_x}{\sqrt{8}}\right)\right]. \end{aligned} \tag{2}$$

In this expression,

$$d_{\text{eff}} = \begin{cases} C_1 d, & x \le -h \\ 0, & -h < x < 0 \\ C_2 d, & x \ge 0 \end{cases},$$

in which C_1 and C_2 are normalized nonlinear coefficients of materials. d is the larger one of the nonlinear coefficients at two sides of the boundary. Besides, h is the width of a tiny gap that might exist in a practical experimental process. $D\left(iak_x/\sqrt{8}\right)$ and $D\left(\sqrt{2}h/a + iak_x/\sqrt{8}\right)$ are Dawson functions. For ideal condition, $h = 0$, so Eq. (2) can be simplified as

$$\begin{aligned} &\int_{-\infty}^{+\infty} d_{\text{eff}} e^{-2x^2/a^2} e^{ik_x x} dx \\ &= d\left[(C_1+C_2)\sqrt{\frac{\pi}{8}} a e^{-a^2k_x^2/8}\right. \\ &\left. + (C_2 - C_1)\frac{a}{\sqrt{2}} e^{-a^2k_x^2/4} D\left(\frac{iak_x}{\sqrt{8}}\right)\right]. \end{aligned} \tag{3}$$

In the case of a single-crystal surface, $C_1 = 0$. In the case of crystal interior, d_{eff} is a constant ($C_1 = C_2 = 1$) and Eq. (3) can be simplified as

$$\int_{-\infty}^{+\infty} d_{\text{eff}} e^{-2x^2/a^2} e^{ik_x x} dx = d_{\text{eff}} \sqrt{\frac{\pi}{2}} a e^{-a^2k_x^2/8}. \tag{4}$$

In Eq. (1), the value of Δk and k_x would vary according to different phase-matching schemes. In the case of normal collinear PPM condition, $\Delta k = k_x = 0$. $\Delta k = k_x = k_2 \sin\theta_c$ represents the condition of CSHG at a nonlinear boundary, in which $\theta_c = \arccos(2k_1 \cos\gamma / k_2)$ and γ is the angle between FF beam and boundary, as shown in Fig. 1(a). The nonlinear boundary is composed of two bulk crystals, such as βBBO and MgO:LN. In our experiment, the phase-matching scheme is a noncollinear PPM form, as shown in Fig. 1(b). It is always an isosceles triangle comprised of incident FF wave vector, reflected FF

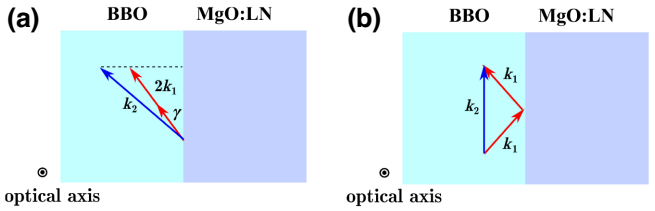

FIG. 1. (a) Phase-matching scheme of CSHG at the interface of BBO and MgO:LN. (b) The noncollinear PPM scheme at the interface of BBO and MgO:LN.

wave vector, and SHG wave vector. In this case, PPM SHG propagates along the interface and the phase-matching condition corresponds to $\Delta k = k_x = 0$.

We simulate and compare the SHG intensities of five cases under the same pumping energy with FF wavelength changing, including collinear PPM inside βBBO, noncollinear PPM based on single BBO surface and BBO-LN interface, and Cherenkov-type phase matching based on a single BBO surface and BBO-LN interface. For noncollinear *oo-e*-type PPM as shown in Fig. 1(b), the nonlinear coefficients are d_{31}^{BBO} (0.16 pm/V) at BBO side [41] and d_{31}^{LN} (4.64 pm/V) at MgO:LN side [42]. In the case of *oo-o*-type CSHG phase matching in Fig. 1(a), the nonlinear coefficients are d_{21}^{BBO} (2.22 pm/V) at the BBO side [41] and d_{31}^{LN} at the MgO:LN side.

The nonlinear conversion efficiency can be represented as $\eta = I_2/I_1 = P_2/P_1$, where $I_1 \propto A_1^2$ is the intensity of the FF beam, P_1 and P_2 represent the pump power and output SHG power in the experiment. Here, we need to compare different frequency-doubling methods under the same pump power and interaction length in the experiment. Therefore, we normalize the pump power P_1 and interaction length z in simulation and data processing. In the later text, the nonlinear conversion efficiency we discuss is normalized.

Figure 2(a) shows SHG efficiencies versus wavelength λ_{SHG} of different phase-matching processes with the same FF intensity ($A_1 = 1$ V/m) and beam radius ($a_0 = 2$ mm). The pump beam is focused with a lens ($f = 100$ mm). Therefore, the beam radius at the focal point can be estimated as $a = 2\lambda_{\mathrm{FF}} f / a_0 = 100\lambda_{\mathrm{FF}}$ in our calculation. In addition, the interaction length of noncollinear SHG can be represented as $z = 2a/\sin\gamma$, so z varies with wavelength and different phase-matching methods. It is necessary to normalize interaction length z in simulation, hence we compare these SHG efficiencies via the values of η/z^2 according to Eq. (1) and the unit of them is mm^{-2}. In Fig. 2(a), the blue dashed curve represents the commonly used *oo-e* type collinear PPM SHG inside BBO crystal according to Eq. (4). The nonlinear conversion efficiency decreases rapidly when the FF wavelength approaches the VUV waveband because of the decreasing d_{eff} according to

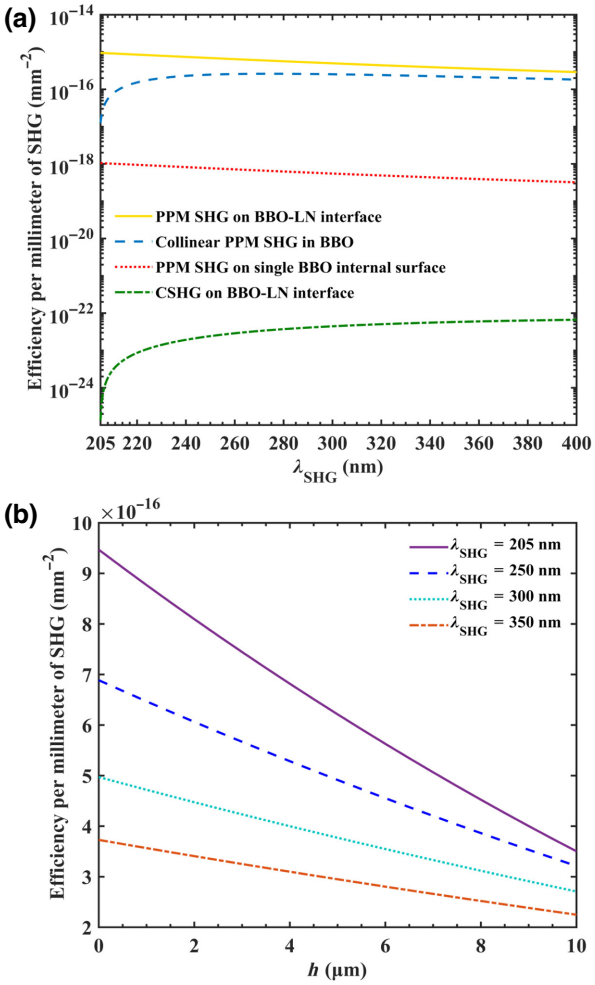

FIG. 2. (a) Efficiency of SHG versus the SHG wavelength from 205 to 400 nm for different phase-matching processes: noncollinear PPM SHG along a BBO-LN interface (no air gap), a single BBO surface, collinear birefringent SHG inside BBO, and CSHG on a BBO-LN interface. (b) Efficiency of noncollinear PPM SHG based on the BBO-LN interface versus the width of air gap between two crystals at 205, 250, 300, and 350 nm, respectively.

Eq. (4). The *oo-o*-type CSHG based on the BBO-LN interface [39] is also calculated as the green dash-dotted curve in Fig. 2(a). The inherent lateral wave-vector mismatching leads to relatively low efficiency of the CSHG. The red dotted and the yellow solid curves are the *oo-e*-type PPM SHG based on a single BBO surface and a BBO-LN interface according to Eq. (3), respectively. According to the simulation in Fig. 2(a), the nonlinear conversion efficiency of the noncollinear PPM method even increases with the wavelength decreasing if neglecting loss. The BBO-LN interface leads to higher efficiency than the single BBO surface. The BBO-LN interface leads to higher efficiency than the single BBO surface. Hence enlarging the difference of $\chi^{(2)}$ at two sides of the nonlinear boundary

is quite necessary. Therefore, higher nonlinear conversion efficiency per unit length becomes the most outstanding advantage of the noncollinear PPM SHG based on the BBO-LN interface according to our simulations. Equation (2) is established according to the nonlinear modulation effect at the boundary, so it mainly reflects the influence on the nonlinearity of this particular region. However, it is really hard to bond two crystals perfectly in practice. Therefore, we further take the influence of air gap between two crystals into consideration. Figure 2(b) shows the efficiency of noncollinear PPM SHG based on the BBO-LN interface versus the width of air gap between two crystals. The purple solid curve, the mandarin blue dashed curve, the cyan dotted curve, and the orange dash-dotted curve correspond to wavelengths of 205, 250, 300, and 350 nm, respectively. The result shows that the existence of air gap will reduce nonlinear conversion efficiency and this effect will be more serious at shorter wavelengths.

III. EXPERIMENT

We compare the SHG intensities of the BBO surface and the BBO-LN interface in the experiments. The size of bulk BBO and 5 mol% MgO:LN, respectively, correspond to $10 \times 5 \times 10$ mm^3 and $10 \times 10 \times 5$ mm^3. The phase-matching scheme we employ in the experiments is illustrated in Fig. 1(b) according to the above theoretical simulations. In this case, SHG is stimulated at the BBO interface.

Figure 3 shows the schematic of the experimental setups. A tunable optical parametric oscillator (approximately ns, 100 Hz) provides the incident FF beam. A half-wave plate (HWP) and a Glan-Taylor prism are used to adjust the polarization and the intensity of the FF beam. A lens with a focal length of 100 mm is used to focus the FF beam into the sample at a particular angle. The diameter of the pump laser is measured as 2 mm, so the diameter of the focused spot is $100\lambda_{FF}$. The expected SHG propagates along the boundary and reaches the detector or screen. The phase-matching angle will vary with FF wavelength, hence samples are put on a rotary stage to change the incident direction (relative to the nonlinear boundary) of the FF beam. The power and wavelength information of the FF beam behind the lens is provided in Appendix A. The UV SHG spot can be recognized via stimulated fluorescence on a paper screen. These UV SHG spots are recorded by a camera. Besides, we also use a UV spectrograph to measure the SHG wavelength. The data obtained via spectrograph are all after intensity calibration. We choose $\lambda_{SHG} = 340$ nm to calibrate spectrum. At this wavelength, the SHG intensity does not exceed the range of measurement of spectrograph, but we can still use power meter to obtain SHG power. We associate the intensity display of spectrograph with the power of SHG, thereby we can confirm the power of SHG at shorter wavelength more accurately assisted by the spectrograph.

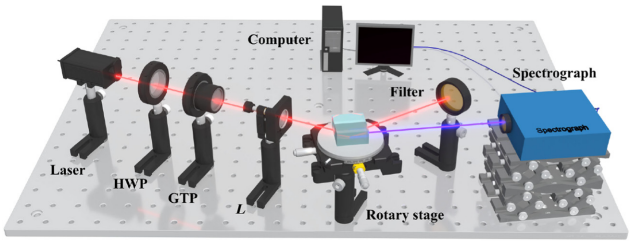

FIG. 3. Schematic of the experimental setup. HWP, half-wave plate; GTP, Glan-Taylor prism; L, the lens with a focal length of 100 mm; sample, βBBO; and 5 mol% MgO : $LiNbO_3$.

Figure 4 shows the experimental results of employing the BBO surface and the BBO-LN interface under the same pump power. The center bluish violet spots in Figs. 4(a)–4(f) are the expected PPM SHGs. The background color is influenced by FF. The contrasts of SHG brightness in Figs. 4(a)–4(c) and Figs. 4(d)–4(f) indicate higher conversion efficiency based on the BBO-LN interface. We also compare the nonlinear conversion efficiencies of these two noncollinear PPM SHGs after normalizing the pump power and interaction length. In Fig. 4(g), the yellow circle marks and red X marks represent the efficiencies of noncollinear PPM SHG generated from the BBO-LN interface and the BBO surface, respectively. The former is generally higher than the latter from 302.5 to 400 nm. This is in agreement with theoretical analysis. There are always pump energy fluctuations when we record P_1 and P_2, so the efficiencies fluctuate, too. Among the results of noncollinear PPM SHG of BBO surface, 302.5 nm is almost the shortest output SHG wavelength we could capture by power meter and spectrograph in the experiment. But for the BBO-LN interface, the SHG at 302.5 nm can be recognized clearly. It demonstrates that higher conversion efficiency in the UV band can be realized based on the interface with a larger gap of $\chi^{(2)}$. The average enhancement factor of the BBO-LN interface is 7.7 according to Fig. 4(g). The relatively lower enhancement factor is caused by the width of the inevitable air gap, the absorption of SHG of MgO:LN and the roughness of the interface. The influence of air gap can be easily observed in our experiment. The power of SHG will increase when we increase the pressing force on the two sides of BBO-LN. Besides, newly polished crystals without mechanical and optical damage also work obviously better in SHG enhancement.

Furthermore, Fig. 5 shows the experimental results of the wavelength below 302.5 nm based on the BBO-LN interface. Figures 5(a)–5(e) are experimental results of noncollinear PPM SHG based on the BBO-LN interface at 295, 275, 255, 235, and 215 nm, respectively. The shortest wavelength of observable PPM SHG by the camera is

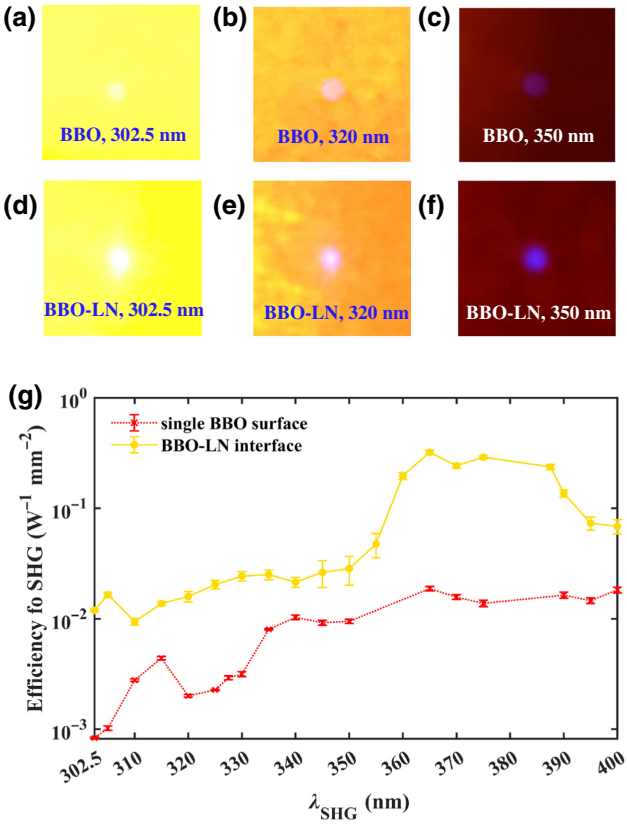

FIG. 4. Experimental comparison of noncollinear PPM SHG based on the single BBO surface and the BBO-LN interface. (a)–(c) and (d)–(f) are, respectively, corresponding to the intensity distribution of noncollinear PPM SHG under the condition of single BBO surface and BBO-LN interface at 302.5, 320, and 350 nm. (g) The measured efficiencies of noncollinear PPM SHGs based on the single BBO surface and the BBO-LN interface.

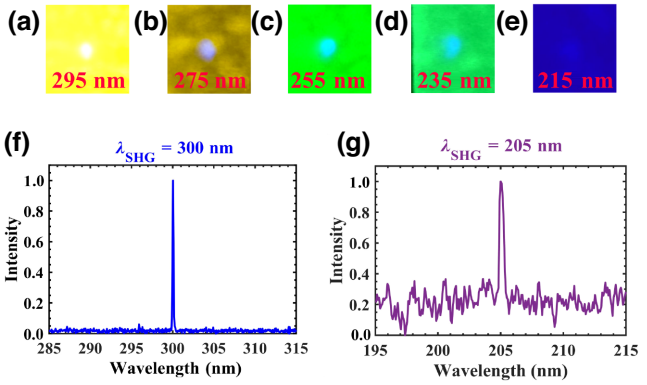

FIG. 5. (a)–(e) The experimental results of noncollinear PPM SHG at 295, 275, 255, 235, and 215 nm based on the BBO-LN interface, respectively. (f),(g) The detected spectrums of noncollinear PPM SHGs at 300 and 205 nm.

215 nm. However, with the λ_{SHG} decreasing, the SH spot gradually becomes difficult to distinguish using a camera due to both the decreasing intensity of SHG and the similar blue color of scattering FF light. Therefore, we employ a spectrograph to detect SHG. Figures 5(f) and 5(g) show the spectrums of SHG at 300 and 205 nm measured by the spectrograph. The shortest wavelength of this noncollinear PPM SHG based on the BBO-LN interface reaches 205 nm, which is also the theoretical limitation of collinear PPM SHG in BBO [29].

As shown in Figs. 4 and 5, the noncollinear PPM SHG based on the nonlinear boundary with a large gap of $\chi^{(2)}$ has good performance to enhance UV SHG. This kind of PPM SHG is also generally more efficient than the CSHG because of lateral phase matching, so it reduces the minimum requirement of pump power and becomes more adaptable for application. Moreover, the high nonlinear conversion efficiency contributed by the small reflection region and the fixed SHG output direction along the boundary make this method valuable in compact UV device design.

In order to compare the efficiencies of the collinear PPM SHG inside BBO with our method, we use a $10 \times 4 \times 3$ mm^3 z-cut bulk βBBO crystal in the experiment. Its polishing surface design is more suitable for birefringence phase matching than the previous BBO. The spectrograph is also exploited to assist measurement. The edge lengths, 10 and 3 mm are applied to calculate the interaction length of this collinear PPM SHG process combined with the incident angle. The conversion efficiencies are plotted as yellow circle marks and blue triangle marks in Fig. 6, respectively. In Fig. 6, we can see that the PPM SHG on the BBO-LN interface still shows higher efficiency. The lack of data of collinear PPM SHG from 212 to 320 nm is caused by the cutting angle of our BBO crystal. The FF light cannot enter the BBO crystal according to Snell's law of interface.

IV. CONCLUSION

To conclude, we demonstrate an efficient PPM SHG method that uses a tightly bonding interface between BBO and MgO:LN to generate UV light. Theoretically, the method we propose is more efficient under the same condition than other normal alternatives, and it even works better at shorter wavelengths. In the experiment, we compare two nonlinear boundaries (single BBO surface and BBO-LN interface) for this kind of PPM SHG. The results verify that we can further enhance PPM SHG by enlarging the nonlinear susceptibility gap at the nonlinear boundary. Our work provides an alternative way for the integrated ultraviolet laser and may promote future UV micromachining development.

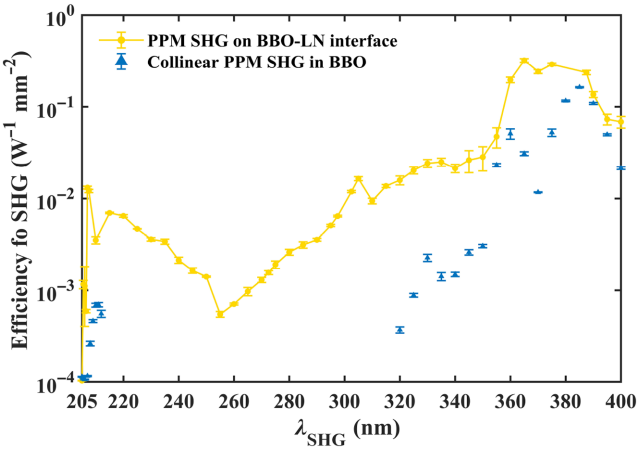

FIG. 6. Measured efficiencies of the noncollinear PPM SHG based on the BBO-LN interface and the collinear PPM SHG inside BBO.

ACKNOWLEDGMENTS

We wish to acknowledge the support of National Key Research and Development Program of China (Grants No. 2018YFA0306301, No. 2017YFA0303701); National Natural Science Foundation of China (Grants No. 11734011, No. 12004245, No. 12074252, No. 62022058); Shanghai Municipal Science and Technology Major Project (Grant No. 2019SHZDZX01-ZX06); Shanghai Rising-Star Program (Grant No. 20QA1405400).

APPENDIX A: POWER OF PUMP PULSES

Figure 7 is the pump power changing with the wavelength.

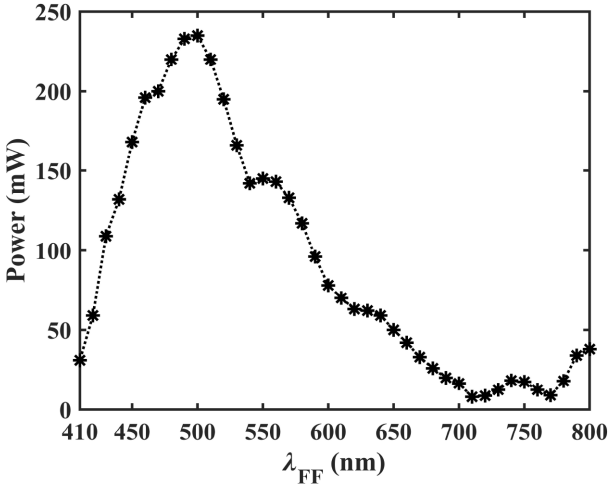

FIG. 7. The measured FF beam power changing with the wavelength.

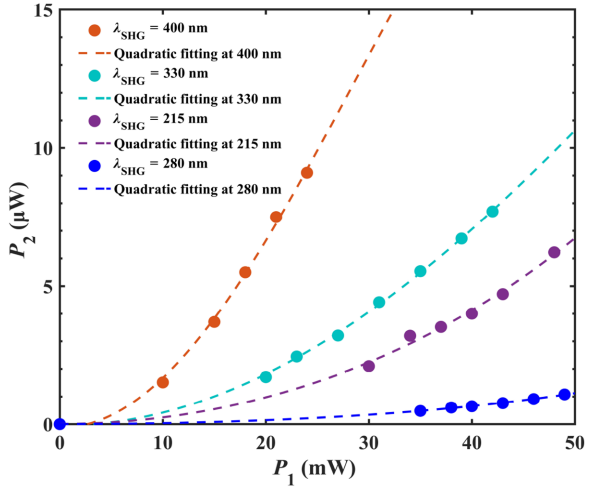

FIG. 8. The SHG power changing with the FF power under the condition of noncollinear PPM based on the BBO-LN interface at 400, 330, 280, and 215 nm, respectively.

APPENDIX B: POWER DEPENDENCE OF PPM SHG BASED ON BBO-LN INTERFACE

We further measure the SHG power changing with the FF power under the condition of noncollinear PPM SHG, as shown in Fig. 8. Circle marks with colors of orange, cyan, mandarin blue, and purple correspond to the results at 400, 330, 280, and 215 nm, respectively. And they are fitted by dashed lines with corresponding colors. Each group of experimental data verifies the relation: $P_2 \propto P_1^2$. This is in agreement with Eqs. (1) and (3).

[1] M. Heßling, K. Hönes, P. Vatter, and C. Lingenfelder, Ultraviolet irradiation doses for coronavirus inactivation–review and analysis of coronavirus photoinactivation studies, GMS Hyg. Infect. Control **15**, Doc08 (2020).

[2] F. Chiappa, B. Frascella, G. P. Vigezzi, M. Moro, L. Diamanti, L. Gentile, P. Lago, N. Clementi, C. Signorelli, N. Mancini, and A. Odone, The efficacy of ultraviolet light-emitting technology against coronaviruses: A systematic review, J. Hosp. Infect. **114**, 63 (2021).

[3] I. Ragan, L. Hartson, H. Pidcoke, R. Bowen, and R. Goodrich, Pathogen reduction of SARS-CoV-2 virus in plasma and whole blood using riboflavin and UV light, PLoS ONE **15**, e0233947 (2020).

[4] J. Bennett, Measuring UV curing parameters of commercial photopolymers used in additive manufacturing, Addit. Manuf. **18**, 203 (2017).

[5] K. Chen, X. Kuang, V. Li, G. Kang, and H. J. Qi, Fabrication of tough epoxy with shape memory effects by UV-assisted direct-ink write printing, Soft Matter **14**, 1879 (2018).

[6] M. S. Alias, M. Tangi, J. A. Holguin-Lerma, E. Stegenburgs, A. A. Alatawi, I. Ashry, R. C. Subedi, D. Priante, M. Khaled. Shakfa, T. K. Ng, and B. S. Ooi,

Review of nanophotonics approaches using nanostructures and nanofabrication for III-nitrides ultraviolet-photonic devices, J. Nanophotonics **12**, 043508 (2018).
[7] V. J. Gómez, M. Graczyk, R. J. Jam, S. Lehmann, and I. Maximov, Wafer-scale nanofabrication of sub-100 nm arrays by deep-UV displacement Talbot lithography, Nanotechnology **31**, 295301 (2020).
[8] X. Zhu, W. Fang, J. Lei, Z. Li, F. Xie, Y. Cao, Y. Zhang, F. Qin, and X. Li, Supercritical lens array in a centimeter scale patterned with maskless UV lithography, Opt. Lett. **45**, 1798 (2020).
[9] L. Sun, H. Zou, and S. Sang, A low-cost and high-efficiency method for four-inch silicon nano-mold by proximity UV exposure, Nanotechnology **33**, 075303 (2021).
[10] C. Thanner and M. Eibelhuber, UV nanoimprint lithography: Geometrical impact on filling properties of nanoscale patterns, Nanomaterials **11**, 822 (2021).
[11] X. Li, R. D. Dupuis, and T. Wernicke, Semiconductor UV photonics: Feature introduction, Photonics Res. **7**, SUVP1 (2019).
[12] J. Leppaniemi, K. Eiroma, H. Majumdar, and A. Alastalo, Far-UV annealed inkjet-printed In_2O_3 semiconductor layers for thin-film transistors on a flexible polyethylene naphthalate substrate, ACS Appl. Mater. Inter. **9**, 8774 (2017).
[13] G. Li, Z. Sun, D. Zhang, Q. Xu, L. Meng, and Y. Qin, Mechanism of sensitivity enhancement of a ZnO nanofilm gas sensor by UV light illumination, ACS Sensors **4**, 1577 (2019).
[14] E. Espid and F. Taghipour, UV-LED photo-activated chemical gas sensors: A review, Crit. Rev. Solid State **42**, 416 (2017).
[15] Q. Lian, W. Sui, X. Wu, F. Yang, and S. Yang, Additive manufacturing of ZrO_2 ceramic dental bridges by stereolithography, Rapid Prototyp. J. **24**, 114 (2018).
[16] W. Huo, X. Zhang, K. Gan, H. Li, S. Yan, Y. Chen, and J. Yang, Ceramic particle-stabilized foams/emulsions with UV light response and further synthesis of ceramic capsules, Chem. Eng. J. **360**, 1459 (2019).
[17] S. H. Ji, D. S. Kim, M. S. Park, and J. S. Yun, Sintering process optimization for 3YSZ ceramic 3D-printed objects manufactured by stereolithography, Nanomaterials **11**, 192 (2021).
[18] J. Østergaard, UV imaging in pharmaceutical analysis, J. Pharmaceut. Biomed. **147**, 140 (2018).
[19] A. J. McGonigle, T. D. Pering, T. C. Wilkes, G. Tamburello, R. D'Aleo, M. Bitetto, A. Aiuppa, and J. R. Willmott, Ultraviolet imaging of volcanic plumes: A new paradigm in volcanology, Geosciences **7**, 68 (2017).
[20] A. Brugger, J. Behmann, S. Paulus, H. G. Luigs, M. T. Kuska, P. Schramowski, K. Kersting, U. Steiner, and A. K. Mahlein, Extending hyperspectral imaging for plant phenotyping to the UV-range, Remote Sens. **11**, 1401 (2019).
[21] E. In, E. Walker, and H. E. Naguib, Novel development of 3D printable UV-curable silicone for multimodal imaging phantom, Bioprinting **7**, 19 (2017).
[22] J. A. Mojeski, M. Almashali, P. Jowdy, M. E. Fitzgerald, K. L. Brady, N. C. Zeitouni, O. R. Colegio, and G. Paragh, Ultraviolet imaging in dermatology, Photodiagnosis Photodyn. Ther. **30**, 101743 (2020).
[23] N. G. Basov, E. M. Balashov, O. V. Bogdankevitch, V. A. Danilychev, G. N. Kashnikov, N. P. Lantzov, and D. D. Khodkevitch, Luminescence of condensed Xe, Kr, Ar and their mixtures in vacuum region of spectrum under excitation by fast electrons, J. Lumin. **1**, 834 (1970).
[24] J. J. Ewing, Excimer laser technology development, IEEE J. Sel. Top. Quantum Electron. **6**, 1061 (2000).
[25] D. Basting and G. Marowsky, *Excimer Laser Technology* (Springer Berlin Heidelberg, 2005).
[26] N. Savage, Ultraviolet lasers, Nat. Photonics **1**, 83 (2007).
[27] S. Nie and Y. Guan, Review of UV laser and its applications in micromachining, Opto-Electron. Eng. **44**, 1169 (2017).
[28] W. Koechner, *Solid-State Laser Engineering* (Springer Berlin Heidelberg, 1992).
[29] T. Sasaki, Y. Mori, M. Yoshimura, Y. Yap, and T. Kamimura, Recent development of nonlinear optical borate crystals: Key materials for generation of visible and UV light, Mater. Sci. Eng. R. Rep. **30**, 1 (2000).
[30] B. Willenberg, F. Brunner, C. R. Phillips, and U. Keller, High-power picosecond deep-UV source via group velocity matched frequency conversion, Optica **7**, 485 (2020).
[31] A. Fragemann, V. Pasiskevicius, and F. Laurell, Second-order nonlinearities in the domain walls of periodically poled $KTiOPO_4$, Appl. Phys. Lett. **85**, 375 (2004).
[32] X. Deng and X. Chen, Domain wall characterization in ferroelectrics by using localized nonlinearities, Opt. Express **18**, 15597 (2010).
[33] H. Ren, X. Deng, Y. Zheng, N. An, and X. Chen, Nonlinear Cherenkov Radiation in an Anomalous Dispersive Medium, Phys. Rev. Lett. **108**, 223901 (2012).
[34] Y. Sheng, V. Roppo, K. Kalinowski, and W. Krolikowski, Role of a localized modulation of $\chi^{(2)}$ in Čerenkov second-harmonic generation in nonlinear bulk medium, Opt. Lett. **37**, 3864 (2012).
[35] V. Roppo, K. Kalinowski, Y. Sheng, W. Krolikowski, C. Cojocaru, and J. Trull, Unified approach to Čerenkov second harmonic generation, Opt. Express **21**, 25715 (2013).
[36] X. Zhao, Y. Zheng, H. Ren, A. Ning, and X. Chen, Surface enhanced nonlinear Cherenkov radiation in one-dimensional nonlinear photonic crystal, Opt. Express **25**, 13897 (2017).
[37] J. Zhang, X. Zhao, Y. Zheng, H. Li, and X. Chen, Universal modeling of second-order nonlinear frequency conversion in three-dimensional nonlinear photonic crystals, Opt. Express **26**, 15675 (2018).
[38] H. Ren, X. Deng, Y. Zheng, N. An, and X. Chen, Enhanced nonlinear Čherenkov radiation on the crystal boundary, Opt. Lett. **38**, 1993 (2013).
[39] X. Zhao, Y. Zheng, N. An, H. Ren, X. Deng, and X. Chen, Enhancement of UV second-harmonic radiation at nonlinear interfaces with discontinuous second-order susceptibilities, Sci. Rep. **8**, 1 (2018).
[40] X. Zhao, Y. Zheng, H. Ren, N. An, X. Deng, and X. Chen, Nonlinear Cherenkov radiation at the interface of two different nonlinear media, Opt. Express **24**, 12825 (2016).
[41] D. N. Nikogosyan, Beta barium borate (BBO), Appl. Phys. A **52**, 359 (1991).
[42] G. D. Boyd, R. C. Miller, K. Nassau, W. L. Bond, and A. Savage, Linbo3: An efficient phase matchable nonlinear optical material, Appl. Phys. Lett. **5**, 234 (1964).